

Article

Investigating a Persistent Stratospheric Aerosol Layer Observed over Southern Europe during 2019

Kalliopi Artemis Voudouri ^{1,2,*}, Konstantinos Michailidis ², Maria-Elissavet Koukouli ² , Samuel Rémy ³, Antje Inness ⁴, Ghassan Taha ^{5,6} , Georgia Peletidou ² , Nikolaos Siomos ⁷, Dimitrios Balis ²  and Mark Parrington ⁴ 

¹ Institute for Astronomy, Astrophysics, Space Applications and Remote Sensing, National Observatory of Athens, 15236 Athens, Greece

² Laboratory of Atmospheric Physics, Physics Department, Aristotle University of Thessaloniki, 54124 Thessaloniki, Greece; komichai@physics.auth.gr (K.M.); mariliza@auth.gr (M.-E.K.); gpeletid@auth.gr (G.P.); balis@auth.gr (D.B.)

³ HYGEOS, 59000 Lille, France; sr@hygeos.com

⁴ European Centre for Medium-Range Weather Forecasts (ECMWF), Reading RG2 9AX, UK; antje.inness@ecmwf.int (A.I.); mark.parrington@ecmwf.int (M.P.)

⁵ Morgan State University, Baltimore, MD 21251, USA; ghassan.taha@nasa.gov

⁶ NASA/GSFC, Greenbelt, MD 20771, USA

⁷ Meteorological Institute, Ludwig Maximilian Universität München (LMU), 80539 Munich, Germany; nikolaos.siomos@physik.uni-muenchen.de

* Correspondence: kavoudou@noa.gr



Citation: Voudouri, K.A.; Michailidis, K.; Koukouli, M.-E.; Rémy, S.; Inness, A.; Taha, G.; Peletidou, G.; Siomos, N.; Balis, D.; Parrington, M.

Investigating a Persistent Stratospheric Aerosol Layer Observed over Southern Europe during 2019. *Remote Sens.* **2023**, *15*, 5394. <https://doi.org/10.3390/rs15225394>

Academic Editors: Yuanjian Yang, Xuan Wang, Longlong Wang, Yun He and Zhenping Yin

Received: 15 September 2023

Revised: 3 November 2023

Accepted: 12 November 2023

Published: 17 November 2023



Copyright: © 2023 by the authors. Licensee MDPI, Basel, Switzerland. This article is an open access article distributed under the terms and conditions of the Creative Commons Attribution (CC BY) license (<https://creativecommons.org/licenses/by/4.0/>).

Abstract: A persistent stratospheric aerosol layer first appeared during July 2019 above Thessaloniki, Greece (40.5°N , 22.9°E). It was initially at 12 km and, during August 2019, was even up to 20 km, with increased thickness and reduced attenuated backscatter levels till the end of the year. In this study, we analyze the geometrical and optical properties of this stratospheric layer, using ground-based Lidar measurements, CALIOP/CALIPSO & OMPS-LP space-borne observations, as well as CAMS/ECMWF assimilation experiments. The main aim of the paper is to present an overview of this atmospheric feature and to identify any temporal changes in the aerosol properties that would signify substantial changes in the composition of this long-lasting stratospheric plume over Thessaloniki. This aim is further enhanced by emphasizing the importance of the combined information based on active ground- and space-borne lidars, passive remote sensing, and models during the complex stratospheric aerosol conditions as those encountered during 2019. The layer's origin is linked to the Raikoke volcanic eruption in the Kuril Islands in June 2019, yielding a particle linear depolarization ratio less than 0.05, while some indications exist that the intense forest fires at mid and high northern latitudes throughout the summer of 2019 also contributed to the persistent layer. We report that in July, mainly volcanic sulphate aerosol layers with a 1–3 km vertical extent were identified in the stratosphere at \sim 15 km over Thessaloniki, while after August and until the end of 2019, the plume heights showed a significant month-to-month variability and a broadening (with thickness greater than 3 km) towards lower altitudes. The aerosol optical thickness was found to be in the range between 0.004 and 0.125 (visible) and 0.001 and 0.095 (infrared) and the particle depolarization of the detected stratospheric plume was found to be 0.03 ± 0.04 , indicative of spherical particles, such as sulphate aerosols.

Keywords: stratospheric layer; remote sensing; Raikoke volcano; CAMS/ECMWF assimilation; space-borne observations

1. Introduction

The impact of stratospheric aerosols in the Earth's radiative budget and ozone burden is widely recognized [1,2]. Their monitoring and characterization are important, not only

for understanding the changes in atmospheric temperature and ozone profiles, but also for their potential use as a geoengineering tool to reduce the impact of global warming [3]. Stratospheric aerosols have a notable impact on global climate due to their long residence time in the stratosphere and their large-scale dispersion [4]. Explosive volcanic eruptions can inject large amounts of ash and sulfur dioxide (SO_2) gas into the lower and middle stratosphere, while volcanic ash can remain in the stratosphere for weeks or, in extreme episodes, for months [5]. Dominated by sulphate aerosols, stratospheric aerosols are typically features extending from the tropopause up to 35 km above sea level (a.s.l.) in the tropics, and about 30 km a.s.l. at midlatitudes [6]. In recent years, there has been evidence that pyrocumulonimbus (PyroCb) events during large wildfires can also inject smoke aerosol into the stratosphere, which can be comparable to volcanic aerosol injections in terms of radiative impact on the stratosphere [7–10].

Several techniques have been reported to monitor the evolution of stratospheric aerosol layers in the literature, including ground-based lidars [11–18], balloon-borne in situ measurements [19], as well as satellite-borne instrumentation [20–23]. The availability of synergistic information from the different instrumentation enhances the retrievals of the spatio-temporal variability and the geometrical, optical, and microphysical properties of the stratospheric features. Ground-based systems provide measurements with high temporal and vertical resolution, whilst satellite-borne instruments can provide global coverage over several years, compensating the generally low signal-to-noise ratio at high altitudes of the ground based lidars.

In the summer of 2019, the Raikoke volcano in the Kuril Islands (48.3°N , 153.3°E) erupted on the 22nd of June, emitting ash and volcanic gases over the North Pacific [24] and releasing around 1.5 Tg SO_2 into the atmosphere [25]. The SO_2 and ash plume rose to around 8–18 km [26,27], resulting in a considerable amount of the SO_2 reaching the stratosphere. Analysis of the CALIOP lidar observations (cloud-aerosol lidar with orthogonal polarization) on board the CALIPSO (Cloud-Aerosol and Lidar Infrared Pathfinder Observations) platform showed that the volcanic plume had circumnavigated the globe by the 30th of August, affecting the stratosphere in the entire northern hemisphere above 30°N [28]. Additionally, intense, record-breaking wildfire activity at high northern latitudes, namely in Alaska, Alberta, and Siberia, was reported during the summer and autumn of 2019 [29,30]. Both types of events can create updrafts strong enough to penetrate the tropopause and it is possible that both sources contributed to the long-lasting observed aerosol plume over Thessaloniki which lasted until the end of 2019.

In this contribution, we discuss the complex stratospheric aerosol conditions that took place above Thessaloniki during the second part of 2019, with simultaneously occurring volcanic and smoke layers. These events are depicted combining different ground and space-based sensing platforms, with the aim of identifying the main source for this long-lasting, but not always stable, stratospheric aerosol layer. The overall purpose of the paper is three-fold: (a) to present an overview of the signatures of the long-lasting stratospheric plume over Thessaloniki, (b) to identify any temporal changes in the aerosol properties indicative of composition changes in the layer, and (c) to emphasize the importance of the combined information based on active ground- and space-borne lidars, passive remote sensing, and models towards trustworthy and complementary global stratospheric aerosol monitoring, given the complex stratospheric aerosol conditions as those encountered during 2019.

The article is structured as follows: the instrumentation and the derived products, along with the methodology adopted for monitoring the stratospheric layer are presented in Section 2. In Section 3, the temporal evolution, the identification of its origin, model simulations, and the geometrical and optical properties of the stratospheric layer are presented, along with the correlative lidar, satellite, and model observations in a case study on July 2019 (pure volcanic sulphate conditions). Finally, Section 4 contains the summary and main conclusions of this article.

2. Instrumentation and Data Products

2.1. THEssaloniki Lidar SYStem (THELISYS)

The intriguing stratospheric features over Thessaloniki for the second part of year 2019 were monitored with THELISYS (Thessaloniki Lidar System), the multi-wavelength lidar system for aerosol characterization designed and operated by the Laboratory of Atmospheric Physics in Aristotle University of Thessaloniki (LAP-AUTH). THELISYS has been part of the European Aerosol Research Lidar Network (EARLINET) [31] since 2000 and currently also part of the aerosols, clouds, and trace gases research infrastructure (ACTRIS; <https://www.actris.eu/>, accessed on 15 November 2023). The system operating during 2019 consisted of three elastic channels at 355, 532, and 1064 nm, two night-time only Raman channels at 387 nm and 607 nm, and two depolarization channels at 532 nm (cross polarized and parallel polarized to the linearly polarized laser beam). The combined use of the analogue and photon-counting mode allows for the retrieval of the aerosol optical and geometrical properties from 800 m up to ~20 km above the ground. The main and basic aerosol optical properties, derivable from the lidar observations, are the particle backscatter coefficient profiles (355, 532, 1064 nm), the particle extinction coefficient profiles (355, 532 nm), the respective extinction-to-backscatter ratio (lidar ratio) at 355 and 532 nm, and the particle linear depolarization ratio (PLDR) at 532 nm. A detailed description of the THELISYS technical characteristics can be found in Siomos et al. [32], whilst a detailed description of the signal processing and the applied algorithms are provided in Voudouri et al. [33]. The THELISYS dataset is regularly analyzed and quality assured (following all the Q/A procedures within EARLINET) and is publicly available at <https://www.earlinet.org/>, accessed on 15 November 2023.

Geometrical and Optical Retrievals with THELISYS

The geometrical boundaries of the stratospheric layer are defined following the methodology of Platt et al. [34]. The layer base altitude is defined as the level at which there is first an increase in signal above the clear background level and of a magnitude equal to 3 times the standard deviation of the background fluctuations. It is further required that the signal continues to increase, or does not decrease, for at least 500 m. This latter requirement ensures that sudden noise “spikes” are not misinterpreted as layer/cloud. The layer top (or effective top) is detected following the same process but moving downward in altitude from the maximum range.

For the optical retrievals and the calculation of the backscatter and extinction coefficient profiles, different approaches are applied to the lidar signals, including the Klett inversion technique [35], the independent determination of the extinction and backscatter coefficients that provides the extinction-to-backscatter ratio; the so-called Raman method [36]; and the transmittance approach [37]. All these techniques require a high enough signal-to-noise ratio (SNR) to cover the stratospheric aerosol layer. In our study, the transmittance approach was applied to the lidar signals at 1064 nm, as the infrared wavelength magnifies the differences in the vertical distribution of the aerosol load, resulting in layers that are easily identified. Cloud-free cases with high SNR were processed for deriving reliable and quantitative results for the geometrical boundaries and the optical properties of the stratospheric layer. An SNR threshold, defined as the lowest altitude where the signal increases above the clear background level by a magnitude of at least 3 times the standard deviation of the background fluctuations, was applied [38], since the lidar signal is strongly attenuated at higher altitude levels and the noisy parts of the signal should be rejected. The layer detection algorithm searches the layer base above the tropopause height that was defined from radiosondes that are released at Thessaloniki airport, twice a day.

The optical depth of the layer can be determined by comparing the backscattering signals just below and above the layer assuming lidar signals correctly represent the scattering medium [37]. Two linear fits of the scattering signals just below and above the layer were applied, permitting the optical depth calculation. Giannakaki et al. [39] used the transmittance method for retrieving the cirrus AOD and compared it with the Klett–Fernald

approach and the Raman method. The sets of independently derived optical depths were in good agreement, with a correlation coefficient of 0.82 for the transmittance/Klett–Fernald comparison and of 0.90 for the Raman/Klett–Fernald comparison.

2.2. CALIPSO/CALIOP Observations and Aerosol Optical Properties and Typing Retrievals

The presence of the stratospheric plume was further monitored during the same period with CALIOP lidar (cloud-aerosol lidar with orthogonal polarization) on board the CALIPSO (Cloud-Aerosol and Lidar Infrared Pathfinder Observations) platform, a dual-wavelength standard backscatter lidar with three measurement channels [40], hereafter CALIPSO. CALIPSO is a joint NASA/CNES (Centre National d’Études Spatiales) satellite, and part of the A-Train orbit (<https://atrain.nasa.gov/>, last access: 15 November 2023), designed to monitor aerosols and clouds at a global scale for improving our understanding of their role in the atmospheric processes. CALIPSO is a sun-synchronous polar orbiting satellite with an equatorial crossing time of around 13:30 LT and approximately 16 days repetition orbit. CALIPSO data consist of three basic types of information: (a) profile products, (b) layer products, and (c) the vertical feature mask (VFM). Profile products provide retrieved extinction and backscatter profiles, layer products provide layer integrated or layer-averaged properties of detected aerosol and cloud layers, and the VFM provides information on cloud and aerosol locations and types. The CALIPSO main observables are the attenuated backscatter coefficients at 532 and 1064 nm and the volume linear depolarization ratio at 532 nm, while the main output is the particle linear depolarization ratio at 532 nm [41]. A more detailed description of the CALIPSO satellite products is available on the NASA website (<https://www-calipso.larc.nasa.gov/documents/>, last access: 15 November 2023). In the study, the Level-2 version 4.20—Standard CALIPSO aerosol layer product (Alay) and the vertical feature mask (VFM) were used.

VFM products were classified into characteristic classes [42], namely into clear air, cloud, aerosol, stratospheric, surface, subsurface, totally attenuated, or invalid feature types. The CALIPSO aerosol-typing scheme is based on the layer-integrated PLDR at 532 nm, that provides critical information related to the particle shape [40,43], and the layer-integrated attenuated backscatter coefficients at 532 and 1064 nm. Additionally, the tropopause height and temperature were considered in the classification. In the V4 version of the CALIPSO algorithm, aerosols are classified into seven subtypes in the troposphere and four subtypes in the stratosphere, namely ash, sulphate/other, smoke, and polar stratospheric aerosol [40]. An updated version, V4.5, of the CALIPSO L2 dataset is described in Tackett et al. [44], which includes an extensive description of the V4.2 stratospheric aerosol subtyping algorithm.

2.3. Space-Borne OMPS-LP Aerosol Extinction Vertical Profiles

Launched on board the Joint Polar Satellite System (JPSS) Suomi National Polar-orbiting Partnership (S-NPP) platform on 28 October 2011, the Ozone Mapping and Profiler Suite (OMPS) Limb Profiler (LP) captures aerosol extinction coefficient profiles with a sampling of ~1 km in altitude and 1.6–1.8 km vertical resolution. OMPS-LP views the atmosphere in a backward direction along the orbit track with three vertical slits, one (central) aligned with the orbit track and the other two (left and right) separated horizontally. In this work, we used the publicly available aerosol Extinction Vertical Profile swath daily 3 slit (AER) V2.1 product [45]. The AER product provides the stratospheric aerosol abundance and evolution at 6 wavelengths (510, 600, 675, 745, 869, and 997 nm) from the cloud top up to 40 km, providing global daily coverage. The OMPS-LP algorithm detects cloud-top height to provide cloud-free and uncleared aerosol products [46,47]. It also provides the stratospheric aerosol optical depths (sAOD) at six wavelengths by integrating the aerosol profile from the tropopause to ~35 km. Taha et al. [48] reported that the V2.0 extinction coefficients at 745, 869, and 997 nm are the most accurate, with relative accuracies and precisions of 10% and 15%, respectively, while the 675 nm relative accuracy and precision is 20%. V2.1 updated the retrieval conversion criteria which improves the aerosol retrieval

at short wavelengths (510–745 nm) and in the presence of fresh volcanic plumes for all wavelengths [49]. OMPS-LP measurements have previously been used to study the global impact of the Raikoke 2019 [28,49–51].

2.4. Stratospheric Composition Modelling

The Copernicus Atmosphere Monitoring Service (CAMS; [52]), operated by the European Centre for Medium-Range Weather Forecasts (ECMWF) on behalf of the European Commission, provides daily SO₂ analyses and 5-day forecasts of volcanic SO₂ in near-real-time [53]. CAMS currently assimilates total column SO₂ products from the GOME-2 instruments on MetOp-B and MetOp-C and the TROPOMI instrument on Sentinel-5P, both of which provide information about the location and strength of volcanic plumes. However, the operational TROPOMI and GOME-2 SO₂ data do not provide any information about the height of the volcanic plumes and, therefore, the SO₂ increments are placed in the mid-troposphere, around 550 hPa or 5 km in the CAMS data assimilation system (operational in Q1/2023).

Inness et al. [53] explored the use of a modified version of the CAMS system that made use of the ESA Sentinel-5p+ Innovation project (S5p + I) TROPOMI SO₂ Layer Height data (LH) [54,55] and found that the forecast skill and the agreement with IASI/Metop retrieved SO₂ altitudes was significantly improved if information about the plume altitude was used. Total column SO₂ maps from one of the experiments using TROPOMI LH data and referred to as LHexp in Inness et al. [53] were used in this study to illustrate the transport of SO₂ from the Raikoke eruption around the Northern Hemisphere (NH) and in the Mediterranean area in the weeks following the eruption, i.e., from 22 June to 29 September 2019.

The operational CAMS model uses a tropospheric chemistry scheme, CB05, which is a modified and extended version of the Carbon Bond 2005 chemistry scheme [56] for the troposphere, as also implemented in the chemical transport model (CTM) TM5 ([57]). The CAMS system is constantly being developed and further enhanced, and one such version is the ICBG. The ICBG results from the coupling of two integrated forecast systems: (i) the IFS-GLOMAP and (ii) the IFS-CB05-BASCOE. The first module is a tropospheric-stratospheric aerosol modal scheme [58] that is embedded in the ECMWF Integrated Forecasting System (IFS), whilst the second one is a tropospheric (IFS-CB05; [57]) and stratospheric (IFS-BASCOE; [59]) chemistry scheme. The coupling of BASCOE and GLOMAP works two-ways: GLOMAP computes the nucleation and condensation of gaseous sulphuric acid onto liquid sulphuric acid particles, as well as the evaporation of liquid sulphuric acid into gaseous state using the prognostic gaseous sulphuric acid concentration from BASCOE and provides the corresponding tendencies to BASCOE. Also, the surface area density (SAD) of the stratospheric aerosol particles as computed by GLOMAP are used in BASCOE for heterogeneous chemistry reactions. The general objective of ICBG is to simulate the aerosol and chemical impact of large volcanic events, using the detailed aerosol microphysical scheme of GLOMAP, the skill of the IFS in simulating tropospheric and stratospheric circulation, and the validated tropospheric and stratospheric global chemistry schemes. In these simulations, only stratospheric sulphate is considered (i.e., no tropospheric sulphate). For this study, time-series of the simulated extinction profile at 532 nm over Thessaloniki were generated with the ICBG (experiment hb4e), along with the simulated total and sulphate AOD.

2.5. Summary of the Datasets Used in This Work

A summary of the technical characteristics of the different instrumentation and modelling results used in this study are provided in Table 1. Table 2 gives an overview of the observational and modelling geophysical parameters used in this work and their contribution to this study.

Table 1. Technical characteristics of the instrumentation and models used in this work.

	Spatial Resolution	Temporal Coverage
THELISYS	7.5 m (1064 nm)	Monday and Thursday following the EARLINET schedule [31]
CALIPSO	Horizontal: 1000 m Vertical: 60 m	16-day repeat cycle
OMPS-LP	Horizontal: ~250 km Vertical: 1.6–1.8 km	16-day repeat cycle
CAMS LHexp	Horizontal: 40 km Vertical: 137 model levels between the surface and 0.01 hPa	6-hourly from 22 June to 29 September 2019
ICBG	Horizontal: 80 km Vertical: 137 model levels between the surface and 0.01 hPa	3-hourly from 1 June to 30 November 2019

Table 2. Summary of the observational and modelling geophysical parameters discussed in this work.

	Geophysical Parameter	Aim in This Paper
THELISYS	Layer top and base altitude Backscatter extinction profiles at 532 and 1064 nm Stratospheric AOD at 1064 nm	Layer temporal evolution, geometrical boundaries, AOD at 1064 nm
CALIPSO	Layer top and base altitude Stratospheric AOD at 532 nm and 1064 nm Particle depolarization ratio at 532 nm Aerosol classification	Geometrical boundaries, AOD at 532 nm, aerosol typing
OMPS-LP	Extinction profile at 997 nm Stratospheric AOD at 997 nm	Layer temporal evolution, AOD at 997 nm
CAMS LHexp	SO ₂ plume [D.U.]	SO ₂ transport around the NH
ICBG	Stratospheric AOD at 550 nm Extinction profile at 550 nm	Layer temporal and spatial evolution, AOD at 550 nm

In short, ground- and space-based datasets were used to monitor the signatures of the atmospheric feature and to identify any temporal changes in the aerosol properties during the 2019 measuring period. The ground-based system provided information on the temporal evolution of the stratospheric layer via its attenuated backscatter profiles and the stratospheric AOD retrievals, with high temporal sampling and high vertical resolution, whilst the correlative CALIPSO and OMPS-LP retrievals, having different temporal coverage, enhanced the spatial sampling by capturing the stratospheric features after the eruption. On top of that, the model simulations suggested the presence of volcanic particles in the stratosphere while the CALIPSO typing scheme identified their origin and their geometrical and optical properties, given the complex atmospheric situation after August 2019.

3. Results and Discussion

The Raikoke volcano erupted around 18:00 UTC on the 22 June 2019 and emitted considerable amounts of SO₂ and ash in a series of explosive events and influenced the aerosol conditions in the lower stratosphere at all latitudes north of about 20°N during the summer and autumn of 2019 [24,49,50,60]. A stratospheric layer was primarily detected by the THELISYS ground-based lidar in July 2019, stimulating the investigation of the main source of this permanent, but not stable, aerosol layer. We further probed the lower stratosphere for this aerosol layer during the period July–December 2019 using space-borne CALIOP/CALIPSO and OMPS-LP observations. The CAMS layer height data assimilation experiment of the Raikoke eruption (referred to as LHexp in the following) also confirmed that the SO₂ plume arrived over the Mediterranean and Thessaloniki station, corroborated by CALIPSO measurements which suggested that the main composition of the layer was

sulphate particles, until August, when local or high northern latitude (i.e., Alaska, Alberta, Siberia) fires also contaminated the lower stratosphere.

An overview of the temporal evolution of the persistent aerosol layer over Thessaloniki as observed by the ground-based lidar measurements, the CAMS Lhexp simulations and the space-borne OMPS-LP observations is discussed in Section 3.1. The identification of the vast majority of the stratospheric aerosols by the CALIPSO typing algorithm are presented in Section 3.2, while the CAMS ICBG stratospheric simulations shown in Section 3.3 further strengthen the previous findings on the sulphate origin of the layer. The geometrical and optical properties of the stratospheric layer, based on ground and space-based observations, are then provided in Section 3.4. One case study, for 25 July 2019, with the combined results of ground, space and simulations is presented and discussed in Section 3.5.

3.1. Temporal Evolution of the Stratospheric Layer

In Figure 1, the evolution of the atmospheric features monitored by THELISYS is presented during the July to October 2019 period. In total, 41 daytime and 17 night-time measurements were performed during this period, out of which 31 cloud-free measurements were analyzed. Figure 1 presents the attenuated scattering ratios at 1064 nm, i.e., the measured 1064 nm attenuated backscatter profiles divided by profiles of molecular attenuated backscatter coefficients (obtained from radiosondes) and calibrated via normalization to the molecular attenuated backscatter value at 8 km. Figure 1 shows that the stratospheric layers first appeared on the 11 July 2019, with a significant month-to-month variability in the plume heights.

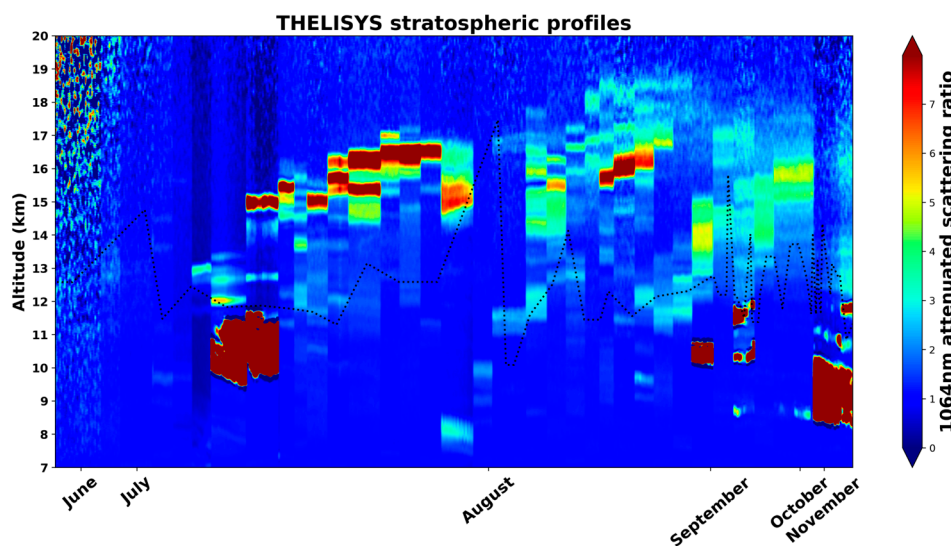


Figure 1. Time–height cross-section of the 1064 nm attenuated scattering ratio retrieved from THELISYS observations between June and November 2019. Cases have been placed one next to the other for visualization purposes. The black dashed line represents the tropopause altitude derived using radiosondes.

On the 1st of August 2019, distinct layers were monitored in similar altitudes but with increased thickness and reduced attenuated backscatter levels. During September, the backscatter levels decreased even further while the layer thickness started growing, while in October, the layer can be seen to extend from 10 to 20 km. Low particle linear depolarization ratios (<0.05 at 532 nm), indicative of spherical particles (i.e., sulphate aerosols), were measured with THELISYS for the whole period.

Figure 2 illustrates the OMPS-LP V2.1 aerosol properties at 997 nm within a box of $\pm 1^\circ$ in latitude and $\pm 25^\circ$ in longitude around Thessaloniki between July and December 2019. In the upper panel, the stratospheric aerosol optical depth is shown, while the bottom panel depicts the extinction-to-molecular ratio, a measure similar to the mixing

ratio. The white dashed line is the tropopause altitude, which identifies possible cloud contamination in the levels below. Similar to the lidar observations (Figure 1), the OMPS-LP first observation of the volcanic plume over Thessaloniki was on the second week of July at ~13 km altitude. The figure shows that the volcanic cloud fully dispersed into the stratosphere over Thessaloniki at the end of August, spreading between the tropopause and ~22 km. The aerosol extinction peaked in September and started decreasing toward the end of the year. OMPS-LP continued to detect volcanic aerosol even after October due to its enhanced sensitivity in the stratosphere [45,50]. Regarding the stratospheric content prior to the eruption, OMPS/LP showed a clean stratosphere from the beginning of year 2019.

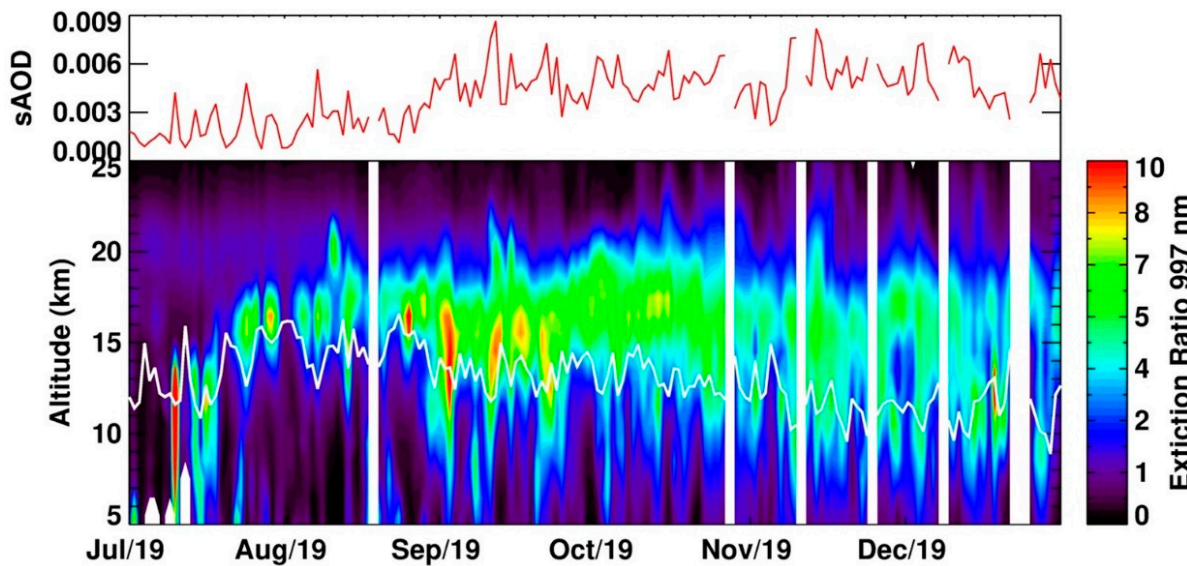


Figure 2. The lower panel depicts a time vs. altitude cross-section of the OMPS-LP aerosol extinction to molecular ratio daily zonal mean profiles at 997 nm within $\pm 1^\circ$ latitude and $\pm 25^\circ$ longitude around Thessaloniki. The white line in the lower panel is the tropopause altitude derived using the NASA Global Modelling and Assimilation Office near-real time atmospheric analyses. White regions indicate no profile was available within the selection criteria. The top panel is the daily zonal mean stratospheric aerosol optical depth (sAOD) at 997 nm.

To further reinforce our premise that the observed features by the ground-based lidar as well as the space-borne OMPS-LP instrument are due to the Raikoke eruption, we show in Figure 3 the temporal evolution of the Raikoke SO₂ plume from the CAMS data assimilation experiment LHexp. This figure illustrates how SO₂ from the eruption was transported around the NH during the month after the eruption till the end of September. Starting in the week after the eruption, upper left, on June 29th the plume of high SO₂ values was located over the Pacific reaching the north American west coast. It reached Europe by July 14th (upper right) where a part of the plume was clearly visible over Greece. A week later (bottom panels), the plume was seen to cover Europe and the Mediterranean, giving rise to sulphate aerosols in the stratosphere of that part of the NH.

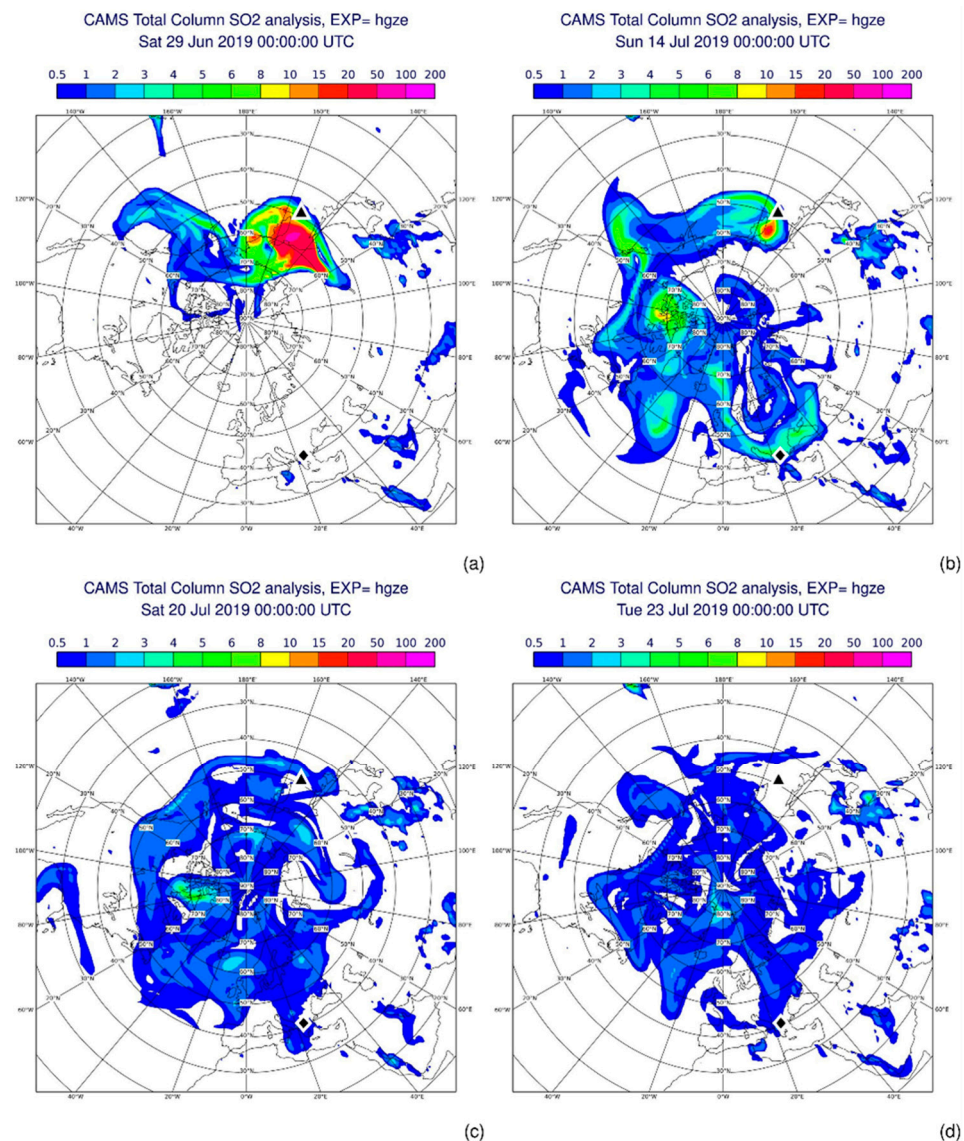


Figure 3. (a–d) CAMS SO₂ total columns (DU) on the 29th of June and 14th, 20th, and 23rd of July 2019 at 00:00 UTC obtained by assimilating (S5p + I) TROPOMI SO₂ layer height the CAMS data assimilation system (LHexp). The triangle marks the location of Raikoke and the diamond the location of Thessaloniki.

3.2. Identification of the Stratospheric Layer Origin Using CALIOP Aerosol Typing

In Figure 4, we present three selected case studies for the 23 July, 26 August, and 12 September 2019, during CALIPSO night-time overpasses. The CALIPSO total attenuated aerosol backscatter at 532 nm as a height–latitude/longitude display is shown on the left column, while on the right column, the CALIPSO aerosol subtype classification from the level 2 vertical feature mask is shown for the three days in question. We should note here that CALIPSO monitors a stable plume extending from the upper troposphere to the stratosphere from the beginning of July till the end of September 2019. For the three example days, the thin blue plumes in the backscatter plots on the left correlate nicely with the dark grey plumes on the right where the CALIPSO VFM algorithms classified the majority of the elevated plumes as stratospheric aerosol layers of subtype 10, i.e., sulphate aerosol, due to their low PLDR values (<0.05).

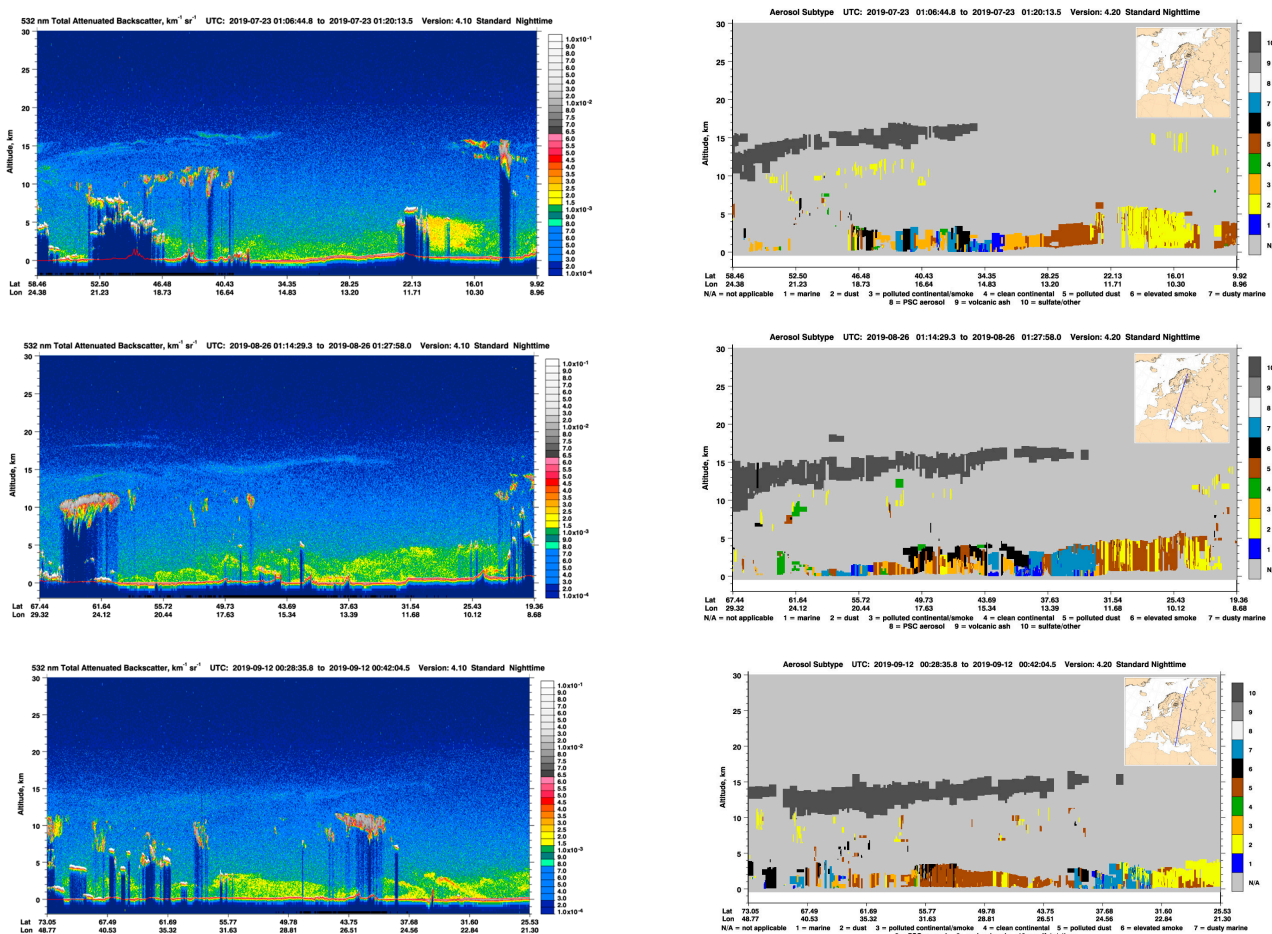


Figure 4. CALIPSO measurement (height–latitude/longitude) display of the total attenuated aerosol backscatter 532 nm (left) and aerosol subtype classification from the level 2 vertical feature mask (right) on 23rd July (first row), 26th August (second row), and 12th September 2019 (third row). Figures adapted from https://www-calipso.larc.nasa.gov/products/lidar/browse_images/std_v4_index.php, last access: 31 August 2023).

As previously noted, CALIPSO retrieves aerosol level 2 data products only where layers were detected and subsequently identified as aerosols. Figure 5 (left) presents the distribution of the aerosol plume, classified as sulphate by the CALIPSO algorithm scheme, against height and latitude, while Figure 5 (right) presents the distribution of the aerosol plume, classified as smoke by the CALIPSO algorithm scheme, against height and latitude. The smoke particles could possibly originate from the Siberian and Canadian fires, and these are nearly always located below the identified sulphate particles, while the more pronounced smoke layers were identified beyond and to the North of Thessaloniki which is at 40°N. The majority of the plume above the tropopause was classified as sulphate (Figure S1), assigned at a frequency of 91.01%, with smoke and ash classifications at rates of 8.79% and 0.2%, respectively, based on the depolarization ratio values. We should note here that smoke misclassifications are expected given the overlap in distributions of the PLDR between the sulphates and the depolarizing smoke regimes as shown in the study of Ansmann et al. [61]. New algorithm improvements are planned to be implemented in the near future, with improved aerosol subtyping in the stratosphere by better accounting for the depolarization thresholds and the assumed lidar ratio values of the observed layers [44].

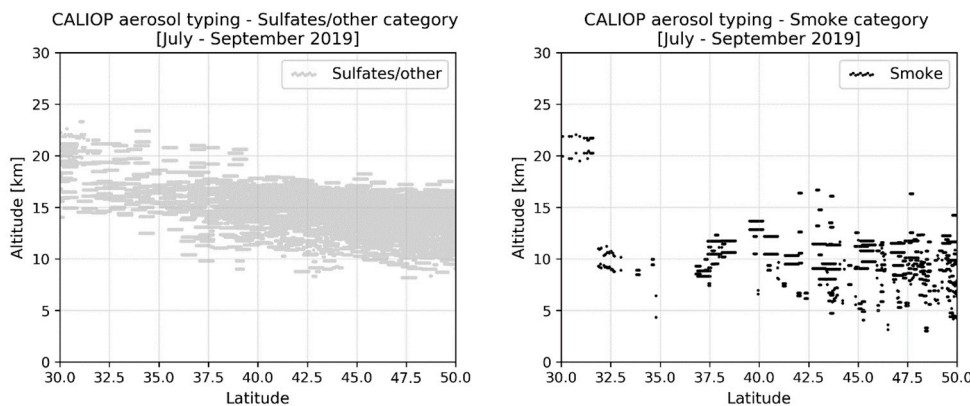


Figure 5. CALIPSO observations of the stratospheric plumes classified as sulfates (**left**) and as smoke (**right**) from July to September 2019 during day and night-time CALIPSO overpasses.

Using model simulations, the OMPS-LP extinction measurements at 869 nm and the Angstrom exponent, also for the Raikoke eruption, Wells et al. [51] showed that including ash in the model simulation provided better agreement with the measurements, indicating that the observed volcanic particles were mostly sulfate mixed with ash.

3.3. Identification of the Stratospheric Layer Origin Using CAMS ICBG Simulations

Time-series of the simulated extinction profiles at 550 nm over Thessaloniki with and without the ICBG experiment hb4e are presented in Figure 6. In the upper left panel, the ICBG simulation without including the Raikoke effect shows a constant stratospheric aerosol extinction profile, while in the upper right panel, the effect of including the Raikoke-induced particles shows clear enhancements in the stratosphere above 10–12 km, increasing as the time-series moves from July to November. In the bottom panel of Figure 6, their difference shows that most of the volcanic aerosol layer is simulated roughly between 12 and 16 km, in agreement with the ground-based THELISYS observations and the OMPS-LP measurements shown previously. Higher extinction values were reported starting around the middle of July 2019, at the time when the CAMS LHeXp showed that the Raikoke SO₂ plume arrived and stabilized over Europe and the Mediterranean region. These high aerosol extinction values remained above their background levels until the end of November 2019.

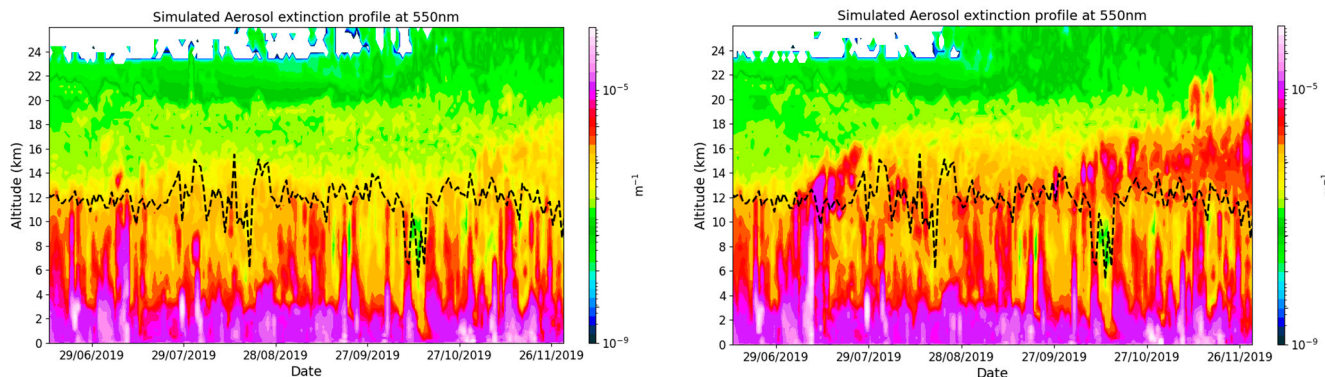


Figure 6. Cont.

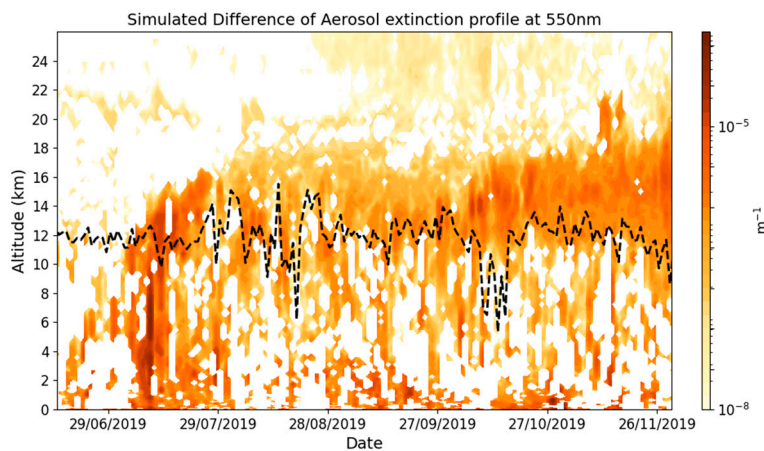


Figure 6. Simulated extinction profile at 550 nm over Thessaloniki without (**upper left**) and with (**upper right**) the Raikoke signal and their absolute differences (**bottom**). The dynamical tropopause height as computed from ERA5 data, provided by Hoffmann et al. [62] is shown in the three panels with a dashed line.

In Figure 7, the associated stratospheric AOD with and without the Raikoke signal from the ICBG experiments is shown as a time-series. The enhancement starting in mid-July, which reappears after October, is more pronounced in this representation and shows how the sulphate AODs remained above their expected background levels.

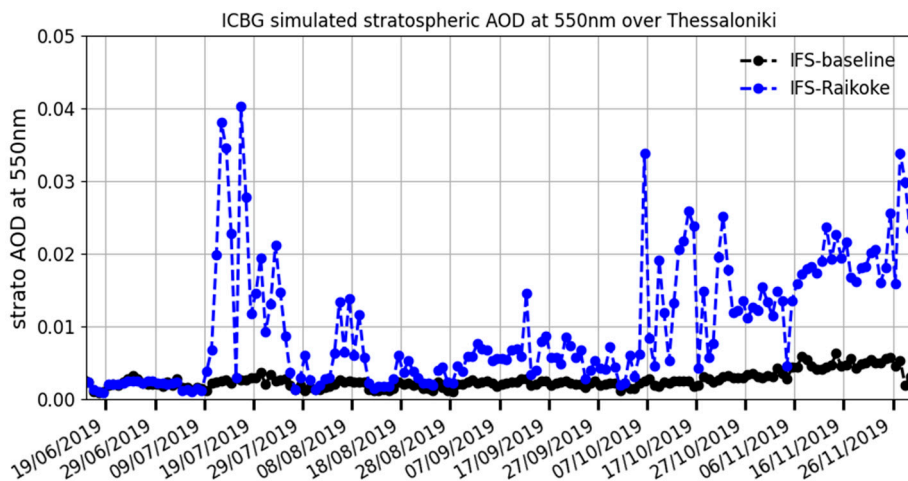


Figure 7. Simulations without (black) and with (blue) the Raikoke eruptions of the stratospheric AOD at 550 nm over Thessaloniki between the 19 June and the 30 November 2019.

3.4. Geometrical and Optical Aerosol Properties from Ground- and Space-Based Measurements

Figure 8 shows the time-series of the THELISYS aerosol layer geometrical thickness and the associated stratospheric AOD values in colors. The geometrical thickness of the stratospheric plume ranged from less than 0.5 km to ~6.5 km, while broader plume layers, with thickness greater than 3 km were observed after August 2019. Optically denser layers, with an infrared AOD mean value of 0.04 ± 0.03 , were also found after mid-August 2019 and early October, possibly linked with the intrusion of smoke particles in the stratosphere and the broadening of the stratospheric layer. The plume thickness remained broad till the end of 2019, exhibiting lower AOD values after November.

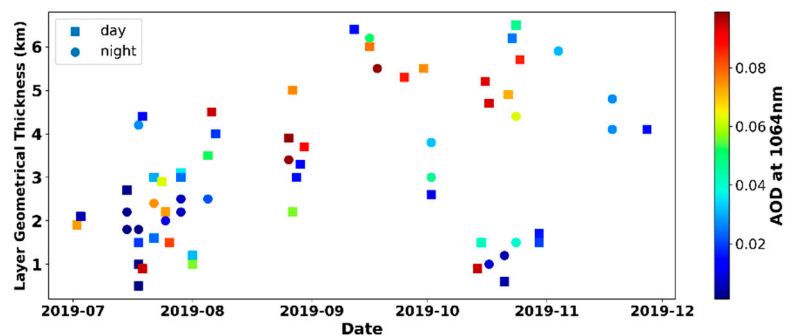


Figure 8. Time-series of the THELISYS aerosol layer geometrical thickness and associated stratospheric AOD [colors]. Square (circle) values correspond to daytime (night-time) retrievals.

Figure 9 (left) illustrates the distribution of THELISYS geometrical boundaries of the observed stratospheric layers, during both day- and night-time measurements, while Figure 9 (right) shows the frequency distribution of the stratospheric AOD column at 1064 nm, from the detected aerosol features. The majority of the detected stratospheric aerosol layers by THELISYS were found in the altitude range between 9.5 and 20 km, with a mean geometrical thickness of 3.2 ± 1.6 km.

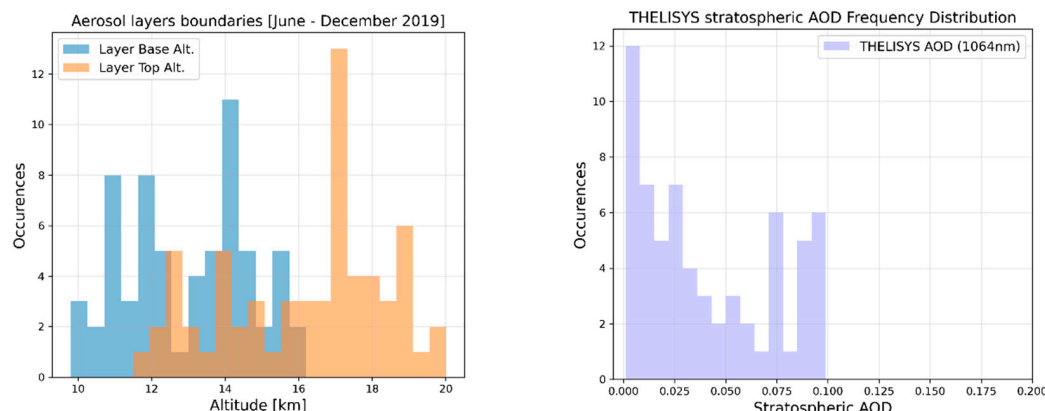


Figure 9. Histogram of the THELISYS night-time stratospheric layer base and layer top boundaries (left) and night-time AOD retrievals at 1064 nm based on the ground-based observations over Thessaloniki (right).

The measured stratospheric AOD at 1064 nm was found to be equal to 0.04 ± 0.03 , with the majority of infrared AODs being at the range between 0.001 and 0.03, exhibiting two peaks, one in the range between 0.001 and 0.008 and the second one between 0.07 and 0.099. The secondary peak observed over Thessaloniki denoting the existence of highly absorbing aerosols was deemed to be a local effect; it could be possibly linked to smoke contamination from local sources.

Additionally, CALIPSO daytime and night-time observations of the stratospheric aerosol features were analyzed for the time period between the 1st of July and the 30th of September 2019 within a broadened selected area along 30° – 50° N and 5° – 35° E (Figure S2). The majority of these cases were night-time overpasses (66 out of 75) and were characterized by a higher SNR compared to daytime retrievals, thus providing higher accuracy in retrieving the boundaries of the aerosol layers as well as their optical properties [42].

Figure 10 illustrates the distribution of the CALIPSO geometrical boundaries of the observed stratospheric layers, during both day and night-time measurements. The majority of the detected stratospheric aerosol layers by CALIPSO were found to be in an altitude range between 8 and 23 km, in accordance with THELISYS retrievals and the plume thickness ranged between 0.4 and 6.4 km with a mean geometrical depth of 1.2 km.

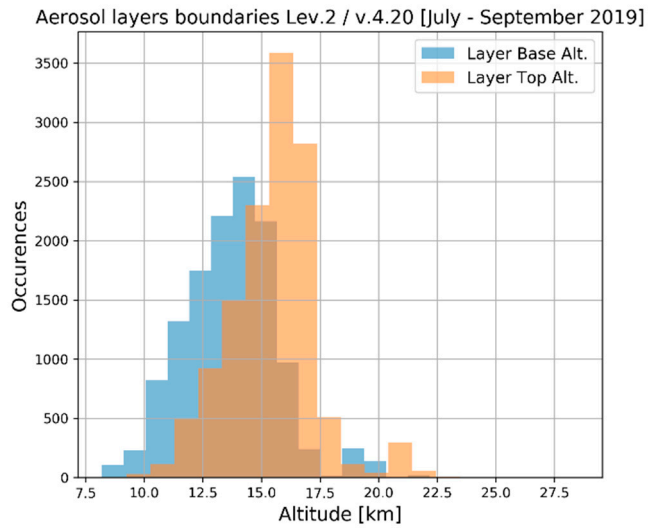


Figure 10. Histogram of CALIPSO “Layer Top” and “Layer Base” boundaries for layers classified as sulphates.

The AOD was retrieved only in the stratospheric region, not including the tropospheric component. Figure 11 (left) shows the frequency distribution of the CALIPSO stratospheric AOD column at 532 nm, whilst Figure 11 (right) shows the frequency distribution of the AOD column at 1064 nm. The mean observed AOD at 532 nm was found to be 0.03 ± 0.026 , while the mean AOD at 1064 nm was found to be 0.006 ± 0.005 . The higher AOD values at 1064 nm observed from THELISYS lidar compared to CALIPSO retrievals could be attributed to contamination of localized smoke particles.

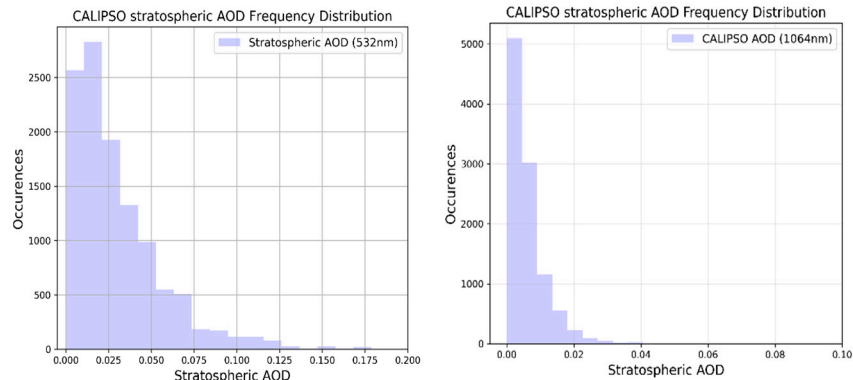


Figure 11. Histogram of the CALIPSO stratospheric AOD at 532 nm (left) and the stratospheric AOD at 1064 nm (right).

The mean particle depolarization ratio of the detected stratospheric layers was found to be 0.03 ± 0.04 (Figure 11 left), indicating the prevalence of a spherical component such as sulphate aerosols. The low PLDR values are consistent with the ground-based THELISYS measurements. Additionally, the calculated Angstrom exponent ranged mostly between 1 and 3 with a mean value of 2.05 ± 1.11 , indicating the presence of smaller particles (Figure 12 right).

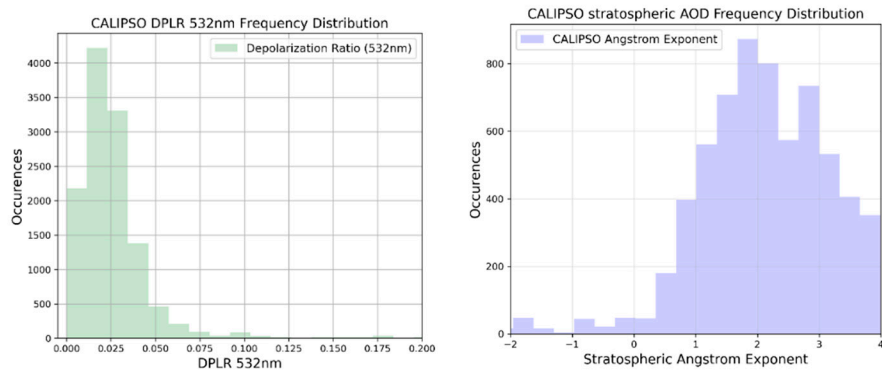


Figure 12. Histogram of CALIPSO frequency distributions of the particle depolarization ratio (**left**) and the stratospheric Angstrom exponent (**right**).

3.5. Correlative Stratospheric Measurements for 25 July 2019

In the current section, a specific day of interest, the 25 July 2019, is presented in detail whereupon all different information sources discussed previously are merged to provide a clear common picture for the stratospheric aerosol plume.

OMPS-LP observations of the stratospheric layer of July 25th, 2019, are presented in Figure 13, showing the volcanic aerosol layer extending between the tropopause altitude and ~ 17.5 km near Thessaloniki (Figure S3).

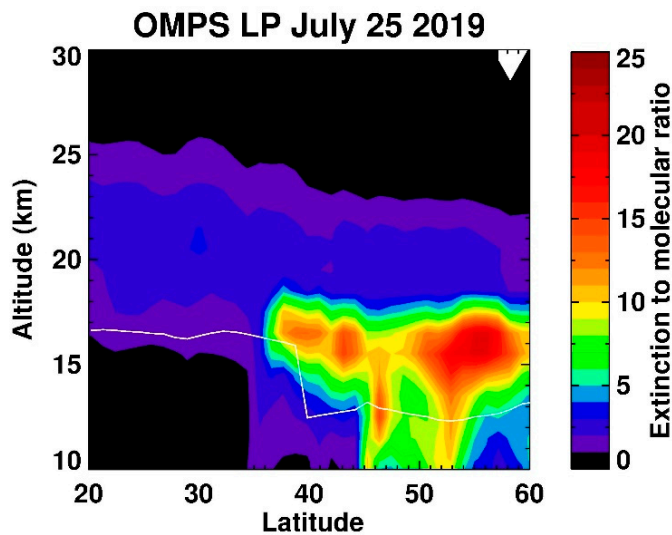


Figure 13. OMPS-LP aerosol extinction to molecular ratio profiles measured on the 25th of July 2019 in longitudes near Thessaloniki and latitudes between 20° and 60° N. The white line denotes the tropopause altitudes, which is included in OMPS-LP daily files and provided by NASA Global Modeling and Assimilation Office (GMAO) [48].

CALIPSO observations of the stratospheric layer for the same date are presented in Figure 14. Two overpasses at close proximity to the ground-based lidar were analyzed; the first one occurred at night (00:44–00:57 UTC) at 60.0 km distance from Thessaloniki and the second one occurred during the day (11:48–12:02 UTC) at 50.0 km (Figure S4). The attenuated backscatter coefficient showed aerosol structures between 15.6 and 16.9 km height from 40° to 43° N during the daytime overpass and between 12.5 and 17.5 km from 39° to 48° N during the night-time overpass (Figure 14a,c).

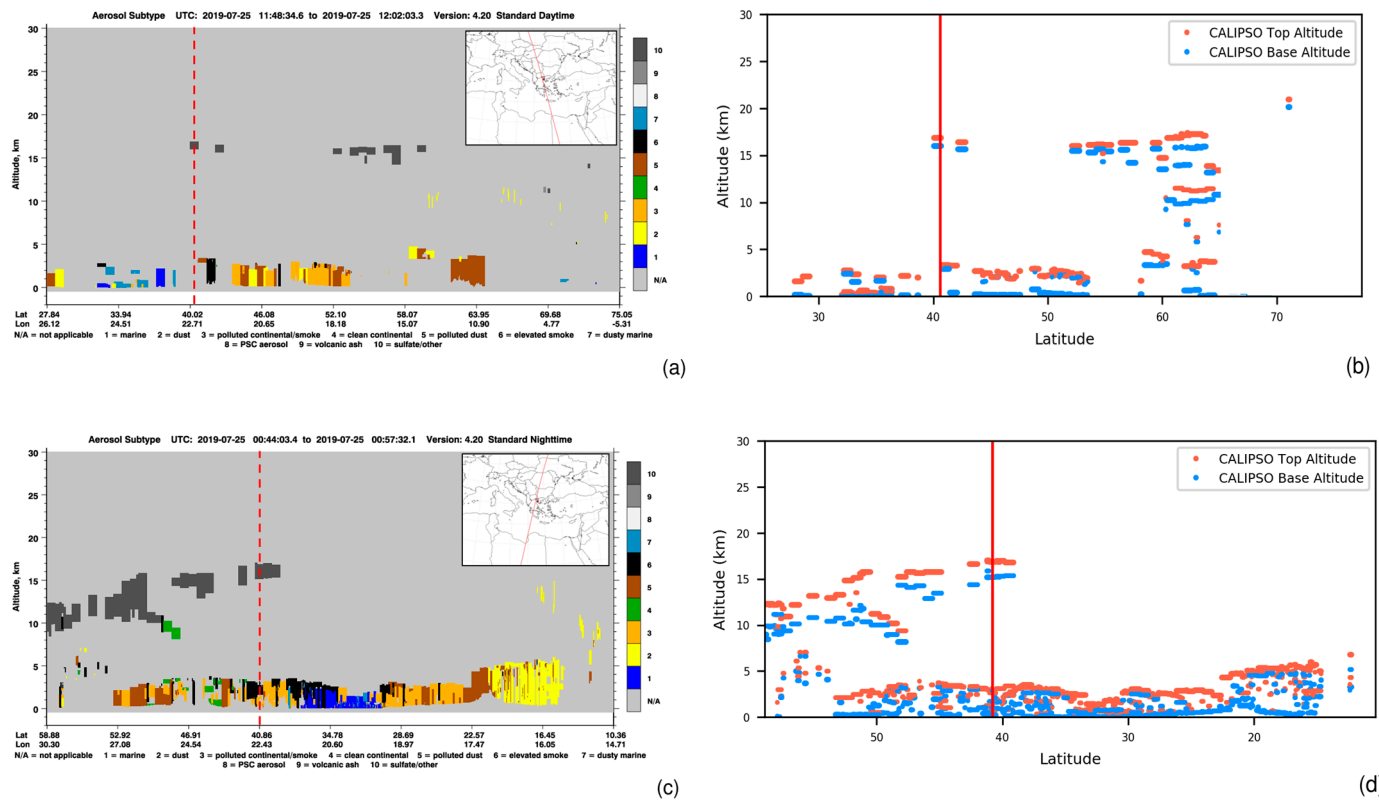


Figure 14. Aerosol layer properties observed by CALIPSO on 25 July 2019 during the daytime (a,b) and night-time (c,d) overpasses across Greece. Aerosol subtyping (a,c) and layer geometrical boundaries (b,d), with top and base altitudes represented as red and blue dots, respectively. Figures adapted from https://www-calipso.larc.nasa.gov/products/lidar/browse_images/std_v4_index.php, last access: 31 August 2023. The red vertical line denotes the closest track point location to Thessaloniki lidar station.

The CALIPSO aerosol typing scheme classified the layer as stratospheric aerosol layer of sulphate type, see dark grey areas in Figure 14a,b. Figure 14b,d show the bottom and top altitude of the detected aerosol plumes. Aerosol heights of the vertically homogeneous sulphate layers were found to range between 12.5 and 17.5 km. These aerosol layers showed low PLDR values at 532 nm ($\text{PLDR} < 0.075$), suggesting the presence of spherical sulphate particles. The total attenuated backscatter values exhibited values of the order of 0.001 to $0.005 \text{ km}^{-1} \cdot \text{sr}^{-1}$ and the mean AOD was found to be 0.023 ± 0.03 at 532 nm and 0.017 at 1064 nm. THELISYS also detected the stratospheric layer at height ranges between 16.2 and 16.8 km. The plume exhibited low PLDR values (< 0.05) and mean AOD values at 532 nm and 1064 nm around 0.012 and 0.0095, respectively.

A summary of the geometrical and optical retrievals from ground observations, space-borne measurements, and model simulations are given in Table 3. For the ICBG experiment and the OMPS-LP observations, a standard Gaussian fit was applied to the profiles provided to calculate the layer's base and top height. All sources denote the presence of the stratospheric plume over Thessaloniki at heights around 16 km, with thicknesses that range from less than 1 km for the THELISYS and the daytime CALIPSO sensing, to ~ 3 km for the OMPS-LP observation. The ICBG hb4e experiment with the Raikoke signal reported a double layer for that day, with the extinction profile at 550 nm showing a weak signal between 10.7 and 12.38 km and a stronger well-defined peak from 14.77 to 16.13 km. The aerosol optical thickness of the detected stratospheric plume was found at the range between 0.009 and 0.023 (visible) and 0.007 and 0.0095 (infrared) and the particle depolarization was found to be less than 0.08, indicating the presence of spherical particles, such as sulphate aerosols.

Table 3. Summary of the stratospheric geometrical, and optical retrievals from 25 July 2019.

THELISYS	CALIPSO		ICBG	OMPS-LP
	Daytime	Night-Time		
<i>Layer Base Height (km)</i>	16.2	16.04	15.40 ± 1.71	14.77
<i>Layer Top Height (km)</i>	16.8	16.44	16.68 ± 1.32	16.13
<i>PLDR</i>	<0.05	0.086	0.018 ± 0.003	n/a
<i>AOD IR (wavelength in nm)</i>	0.0095 (1064)	n/a	0.002 ± 0.006	n/a
<i>AOD VIS (wavelength in nm)</i>	0.012 (532)	0.017 (532)	$0.023 \pm 0.03(532)$	0.009 (550)
				n/a

4. Conclusions

- Complex stratospheric aerosol conditions with simultaneously occurring volcanic and smoke layers took place in the second half of 2019 over Thessaloniki, Greece. A persistent stratospheric layer with variable geometric boundaries (from 10 up to 20 km) was monitored with a Raman lidar over Thessaloniki, Greece, starting from July 2019, stimulating the investigation of the main source of this persistent, but not stable, aerosol layer. We further probed the lower stratosphere for this aerosol layer during the period July–December 2019 using space-borne CALIOP/CALIPSO and OMPS-LP observations. A CAMS data assimilation experiment of the Raikoke eruption also confirmed that the SO₂ plume arrived over the Mediterranean and Thessaloniki station, corroborated by CALIPSO measurements which indicated that the main composition of the layer was sulphate particles. This was until August, when local or high northern latitudes (i.e., Alaska, Alberta, Siberia) fires also contaminated the lower stratosphere. All sensors with different detection limitations captured the temporal and height variability of the observed layer above Thessaloniki during the complex stratospheric aerosol conditions of 2019. In short, the ground-based system monitored the stratospheric layer with high temporal sampling and high vertical resolution, denoting an increased thickness till the end of 2019, whilst the correlative CALIPSO and OMPS-LP retrievals, having different temporal coverage, enhanced the spatial sampling by capturing the stratospheric features after the eruption. On top of that, the model simulations suggested the presence of volcanic particles in the stratosphere and the CALIPSO typing scheme identified the plume's origin and geometrical and optical properties. The combined results of ground measurements, space observations, and model simulations are summarized as follows. The pronounced aerosol layer was present from July 2019 to the end of that year. During July, volcanic sulphate aerosol layers (particle linear depolarization ratio < 0.08) with a 1–3 km vertical extent were mainly identified in the stratosphere over Thessaloniki, while after August, the plume heights showed significant month-to-month variability and a broadening (with thickness greater than 3 km) towards lower altitudes.
- The aerosol optical thickness was found to be in the range between 0.004 and 0.125 (visible) and 0.001 and 0.095 (infrared) and the particle depolarization of the detected stratospheric plume was found to be 0.03 ± 0.04 , indicative of spherical particles such as sulphate aerosols.
- The CALIPSO aerosol-typing identified the volcanic sulphate aerosol type as the dominant type of the stratospheric plume for ~91% of the identified stratospheric layers throughout the year of 2019, whilst a small number of aerosol layers (~9%) were classified as smoke and ash particles, possibly originating from Siberian and Canadian fires. The smoke particles were nearly always located below the identified sulphate particles, while the more pronounced smoke layers were identified beyond and to the North of Thessaloniki.
- The consistency of the active and passive measurements and CAMS assimilations was identified for the case study of the 25 July. The case presented, in detail, the geometrical boundaries (~16 km) and the optical signature of the stratospheric plume

from the different sources and the CALIPSO aerosol-typing identified the volcanic sulphate aerosol type as the predominant type of the stratospheric plume.

We aim to apply the main lessons and insights stemming from this study to the ongoing severe 2023 fire season in Greece. From the lidar observations, we aim to apply a novel aerosol species separation algorithm on the THELISYS observations, designed to retrieve vertical concentration profiles of individual aerosol species by combining measurements from lidar systems and spectrophotometers [63]. Pure, as well as mixed aerosol types can be identified which will greatly enable future in-depth studies of the aerosol layers reaching Thessaloniki. The OMPS-LP observations should also be further exploited by calculating the aerosol particle mode radius which, alongside the Ångström exponent, will allow determination of the particles' nature with more confidence.

While the differences in spatial resolution, temporal availability, and spectral ranges of the different observational, as well as simulation datasets is irrefutable, the synergistical analysis of ground-based, space-borne, and modelling outputs can only benefit their assimilation into climate and Earth-system models, to account for the impact of stratospheric features and the aerosol–cloud interactions for long-term climate work.

Supplementary Materials: The following supporting information can be downloaded at: <https://www.mdpi.com/article/10.3390/rs15225394/s1>.

Author Contributions: Conceptualization, D.B., N.S., K.A.V. and M.-E.K.; data curation, K.A.V., K.M., A.I., S.R., G.T. and G.P.; writing—original draft preparation, K.A.V.; writing—review and editing, M.-E.K. and M.P. All authors have read and agreed to the published version of the manuscript.

Funding: This research was financially supported by PANGEA4CalVal (Grant Agreement 101079201)

funded by the European Union .

Data Availability Statement: The ground-based lidar data used in this study are available upon registration at <http://data.earlinet.org>, accessed on 15 November 2023. The CALIPSO data were obtained from the online archive of the NASA Langley Research Center Atmospheric Science Data Center (ASDC, <https://asdc.larc.nasa.gov/project/CALIPSO>; last access: 15 November 2023). The OMPS-LP aerosol profiles are publicly available from the NASA EarthData repository (https://disc.gsfc.nasa.gov/datasets/OMPS_NPP_LP_L2_AER_DAILY_2/summary; last access: 15 November 2023). The DOI of the CAMS LHexp used in this paper is <https://doi.org/10.21957/jraa-s174>.

Acknowledgments: The Copernicus Atmosphere Monitoring Service is operated by the European Centre for Medium-Range Weather Forecasts on behalf of the European Commission as part of the Copernicus Programme (<http://copernicus.eu>, accessed on 15 November 2023). The results presented in this work have been produced using the Aristotle University of Thessaloniki (AUTH) High Performance Computing Infrastructure and Resources. MEK would like to acknowledge the support provided by the AUTH IT Center throughout the progress of this research work.

Conflicts of Interest: The authors declare no conflict of interest.

References

- Thompson, D.W.; Solomon, S. Understanding recent stratospheric climate change. *J. Clim.* **2009**, *22*, 1934–1943. [[CrossRef](#)]
- Domeisen, D.I.V.; Butler, A.H. Stratospheric drivers of extreme events at the Earth's surface. *Commun. Earth Env.* **2020**, *1*, 59. [[CrossRef](#)]
- Rasch, P.J.; Tilmes, S.; Turco, R.P.; Robock, A.; Oman, L.; Chen, C.-C.; Stenchikov, G.L.; Garcia, R.R. An overview of geoengineering of climate using stratospheric sulphate aerosols. *Philos. Trans. R. Soc. A* **2008**, *366*, 4007–4037. [[CrossRef](#)] [[PubMed](#)]
- Hofmann, D.; Barnes, J.; O'Neill, M.; Trudeau, M.; Neely, R. Increase in background stratospheric aerosol observed with lidar at Mauna Loa Observatory and Boulder, Colorado. *Geophys. Res. Lett.* **2009**, *36*, L15808. [[CrossRef](#)]
- Vernier, J.-P.; Fairlie, T.D.; Deshler, T.; Natarajan, M.; Knepp, T.; Foster, K.; Wienhold, F.G.; Bedka, K.M.; Thomason, L.; Trepte, C. In situ and space-based observations of the Kelud volcanic plume: The persistence of ash in the lower stratosphere. *J. Geophys. Res. Atmos.* **2016**, *121*, 11104–11118. [[CrossRef](#)] [[PubMed](#)]
- Kremser, S.; Thomason, L.W.; von Hobe, M.; Hermann, M.; Deshler, T.; Timmreck, C.; Toohey, M.; Stenke, A.; Schwarz, J.P.; Weigel, R.; et al. Stratospheric aerosol—Observations, processes, and impact on climate. *Rev. Geophys.* **2016**, *54*, 278–335. [[CrossRef](#)]

7. Fromm, M.; Lindsey, D.T.; Servranckx, R.; Yue, G.; Trickl, T.; Sica, R.; Doucet, P.; Godin-Beekmann, S. The untold story of pyrocumulonimbus. *Bull. Am. Meteorol. Soc.* **2010**, *91*, 1193–1209. [[CrossRef](#)]
8. Peterson, D.A.; Campbell, J.R.; Hyer, E.J.; Fromm, M.D.; Kablick, G.P.; Cossuth, J.H.; DeLand, M.T. Wildfire-driven thunderstorms cause a volcano-like stratospheric injection of smoke. *NPJ Clim. Atmos. Sci.* **2018**, *2018*, 30. [[CrossRef](#)]
9. Yu, P.; Toon, O.B.; Bardeen, C.G.; Zhu, Y.; Rosenlof, K.H.; Portmann, R.W.; Thornberry, T.D.; Gao, R.; Davis, S.M.; Wolf, E.T.; et al. Black carbon lofts wildfire smoke high into the stratosphere to form a persistent plume. *Science* **2019**, *365*, 587–590. [[CrossRef](#)]
10. Torres, O.; Bhartia, P.K.; Taha, G.; Jethva, H.; Das, S.; Colarco, P.; Krotkov, N.; Omar, A.; Ahn, C. Stratospheric Injection of Massive Smoke Plume from Canadian Boreal Fires in 2017 as seen by DISCOVR-EPIC, CALIOP and OMPS-LP Observations. *J. Geophys. Res.-Atmos.* **2020**, *125*, e2020JD032579. [[CrossRef](#)]
11. Mattis, I.; Siefert, P.; Müller, D.; Tesche, M.; Hiebsch, A.; Kanitz, T.; Schmidt, J.; Finger, F.; Wandinger, U.; Ansmann, A. Volcanic aerosol layers observed with multiwavelength Raman lidar over central Europe in 2008–2009. *J. Geophys. Res.-Atmos.* **2010**, *115*, D00L04. [[CrossRef](#)]
12. Pappalardo, G.; Wandinger, U.; Mona, L.; Hiebsch, A.; Mattis, I.; Amodeo, A.; Ansmann, A.; Seifert, P.; Linné, H.; Apituley, A.; et al. EARLINET correlative measurements for CALIPSO: First intercomparison results. *J. Geophys. Res.* **2010**, *115*, D00H19. [[CrossRef](#)]
13. Sicard, M.; Guerrero-Rascado, J.L.; Navas-Guzmán, F.; Preisler, J.; Molero, F.; Tomás, S.; Bravo-Aranda, J.A.; Comerón, A.; Rocadenbosch, F.; Wagner, F.; et al. Monitoring of the Eyjafjallajökull volcanic aerosol plume over the Iberian Peninsula by means of four EARLINET lidar stations. *Atmos. Chem. Phys.* **2012**, *12*, 3115–3130. [[CrossRef](#)]
14. Trickl, T.; Giehl, H.; Jäger, H.; Vogelmann, H. 35 yr of stratospheric aerosol measurements at Garmisch-Partenkirchen: From Fuego to Eyjafjallajökull, and beyond. *Atmos. Chem. Phys.* **2013**, *13*, 5205–5225. [[CrossRef](#)]
15. Khaykin, S.M.; Godin-Beekmann, S.; Keckhut, P.; Hauchecorne, A.; Jumelet, J.; Vernier, J.-P.; Bourassa, A.; Degenstein, D.A.; Rieger, L.A.; Bingen, C.; et al. Variability and evolution of the midlatitude stratospheric aerosol budget from 22 years of ground-based lidar and satellite observations. *Atmos. Chem. Phys.* **2017**, *17*, 1829–1845. [[CrossRef](#)]
16. Boselli, A.; Scollo, S.; Leto, G.; Sanchez, R.Z.; Sannino, A.; Wang, X.; Coltellini, M.; Spinelli, N. First volcanic plume measurements by an elastic/raman lidar close to the Etna summit craters. *Front. Earth Sci.* **2018**, *6*, 125. [[CrossRef](#)]
17. Zuev, V.V.; Burlakov, V.D.; Nevezorov, A.V.; Pravdin, V.L.; Savelieva, E.S.; Gerasimov, V.V. 30-year lidar observations of the stratospheric aerosol layer state over Tomsk (Western Siberia, Russia). *Atmos. Chem. Phys.* **2017**, *17*, 3067–3081. [[CrossRef](#)]
18. Ansmann, A.; Tesche, M.; Seifert, P.; Groß, S.; Freudenthaler, V.; Apituley, A.; Wilson, K.M.; Serikov, I.; Linné, H.; Heinold, B.; et al. Ash and fine-mode particle mass profiles from EARLINET-AERONET observations over central Europe after the eruptions of the Eyjafjallajökull volcano in 2010. *J. Geophys. Res.-Atmos.* **2011**, *116*, D00U02. [[CrossRef](#)]
19. Deshler, T.; Hervig, M.; Hofmann, D.; Rosen, J.; Liley, J. Thirty years of in situ stratospheric aerosol size distribution measurements from Laramie, Wyoming (41N), using balloon-borne instruments. *J. Geophys. Res.-Atmos.* **2003**, *108*, 4167. [[CrossRef](#)]
20. Vernier, J.P.; Pommereau, J.P.; Garnier, A.; Pelon, J.; Larsen, N.; Nielsen, J.; Christensen, T.; Cairo, F.; Thomason, L.W.; Leblanc, T.; et al. Tropical stratospheric aerosol layer from CALIPSO lidar observations. *J. Geophys. Res.-Atmos.* **2009**, *114*, D4. [[CrossRef](#)]
21. Toledo, C.; Bennouna, Y.; Cachorro, V.; Ortiz de Galisteo, J.P.; Stohl, A.; Stebel, K.; Kristiansen, N.I.; Olmo, F.J.; Lyamani, H.; Obregón, M.A.; et al. Aerosol properties of the Eyjafjallajökull ash derived from sun photometer and satellite observations over the Iberian Peninsula. *Atmos. Environ.* **2012**, *48*, 22–32. [[CrossRef](#)]
22. Chouza, F.; Leblanc, T.; Barnes, J.; Brewer, M.; Wang, P.; Koon, D. Long-term (1999–2019) variability of stratospheric aerosol over Mauna Loa, Hawaii, as seen by two co-located lidars and satellite measurements. *Atmos. Chem. Phys.* **2020**, *20*, 6821–6839. [[CrossRef](#)]
23. McCormick, M.; Veiga, R. SAGE II measurements of early Pinatubo aerosols. *Geophys. Res. Lett.* **1992**, *19*, 155–158. [[CrossRef](#)]
24. Vaughan, G.; Wareing, D.; Ricketts, H. Measurement Report: Lidar Measurements of Stratospheric Aerosol Following the 2019 Raikoke and Ulawun Volcanic Eruptions. *Atmos. Chem. Phys.* **2021**, *21*, 5597–5604. [[CrossRef](#)]
25. de Leeuw, J.; Schmidt, A.; Witham, C.S.; Theys, N.; Taylor, I.A.; Grainger, R.G.; Pope, R.J.; Haywood, J.; Osborne, M.; Kristiansen, N.I. The 2019 Raikoke volcanic eruption—Part 1: Dispersion model simulations and satellite retrievals of volcanic sulfur dioxide. *Atmos. Chem. Phys.* **2021**, *21*, 10851–10879. [[CrossRef](#)]
26. Muser, L.O.; Hoshyaripour, G.A.; Bruckert, J.; Horváth, Á.; Malinina, E.; Wallis, S.; Prata, F.J.; Rozanov, A.; von Savigny, C.; Vogel, H.; et al. Particle aging and aerosol–radiation interaction affect volcanic plume dispersion: Evidence from the Raikoke 2019 eruption. *Atmos. Chem. Phys.* **2020**, *20*, 15015–15036. [[CrossRef](#)]
27. Grebennikov, V.S.; Zubachev, D.S.; Korshunov, V.A.; Sakhibgareev, D.G.; Chernikh, I.A. Observations of Stratospheric Aerosol at Rosgidromet Lidar Stations after the Eruption of the Raikoke Volcano in June 2019. *Atmos. Ocean. Opt.* **2020**, *33*, 519–523. [[CrossRef](#)]
28. Khaykin, S.M.; de Laat, A.T.J.; Godin-Beekmann, S.; Hauchecorne, A.; Ratynski, M. Unexpected self-lofting and dynamical confinement of volcanic plumes: The Raikoke 2019 case. *Sci. Rep.* **2022**, *12*, 22409. [[CrossRef](#)]
29. Ohneiser, K.; Ansmann, A.; Chudnovsky, A.; Engelmann, R.; Ritter, C.; Veselovskii, I.; Baars, H.; Gebauer, H.; Griesche, H.; Radenz, M.; et al. The unexpected smoke layer in the High Arctic winter stratosphere during MOSAiC 2019–2020. *Atmos. Chem. Phys.* **2021**, *21*, 15783–15808. [[CrossRef](#)]
30. Junghenn Noyes, K.T.; Kahn, R.A.; Limbacher, J.A.; Li, Z. Canadian and Alaskan wildfire smoke particle properties, their evolution, and controlling factors, from satellite observations. *Atmos. Chem. Phys.* **2022**, *22*, 10267–10290. [[CrossRef](#)]

31. Pappalardo, G.; Amodeo, A.; Apituley, A.; Comeron, A.; Freudenthaler, V.; Linné, H.; Ansmann, A.; Bösenberg, J.; D’Amico, G.; Mattis, I.; et al. EARLINET: Towards an advanced sustainable European aerosol lidar network. *Atmos. Meas. Tech.* **2014**, *7*, 2389–2409. [CrossRef]
32. Siomos, N.; Balis, D.S.; Voudouri, K.A.; Giannakaki, E.; Filioglou, M.; Amiridis, V.; Papayannis, A.; Frakos, K. Are EARLINET and AERONET climatologies consistent? The case of Thessaloniki, Greece. *Atmos. Chem. Phys.* **2018**, *18*, 11885–11903. [CrossRef]
33. Voudouri, K.A.; Siomos, N.; Michailidis, K.; D’Amico, G.; Mattis, I.; Balis, D. Consistency of the Single Calculus Chain Optical Products with Archived Measurements from an EARLINET Lidar Station. *Remote Sens.* **2020**, *12*, 3969. [CrossRef]
34. Platt, C.M.R.; Young, S.A.; Carswell, A.I.; Pal, S.R.; McCormick, M.P.; Winker, D.M.; DelGusta, M.; Stefanutti, L.; Eberhard, W.L.; Hardesty, M.; et al. The experimental cloud lidar pilot study (ECLIPS) for cloud-radiation research. *Bull. Am. Meteorol. Soc.* **1994**, *75*, 1635–1654. [CrossRef]
35. Klett, J.D. Lidar inversion with variable backscatter to extinction ratios. *Appl. Opt.* **1985**, *24*, 1638–1643. [CrossRef]
36. Ansmann, A.; Riebesell, M.; Weitkamp, C. Measurement of atmospheric aerosol extinction profiles with a Raman lidar. *Opt. Lett.* **1990**, *15*, 746–748. [CrossRef]
37. Chen, W.N.; Chiang, C.W.; Nee, J.B. Lidar ratio and depolarization ratio for cirrus clouds. *Appl. Opt.* **2002**, *41*, 6470–6476. [CrossRef]
38. Voudouri, K.A.; Giannakaki, E.; Komppula, M.; Balis, D. Variability in cirrus cloud properties using a PollyXT Raman lidar over high and tropical latitudes. *Atmos. Chem. Phys.* **2020**, *20*, 4427–4444. [CrossRef]
39. Giannakaki, E.; Balis, D.S.; Amiridis, V.; Kazadzis, S. Optical and geometrical characteristics of cirrus clouds over a Southern European lidar station. *Atmos. Chem. Phys.* **2007**, *7*, 5519–5530. [CrossRef]
40. Winker, D.M.; Vaughan, M.A.; Omar, A.; Hu, Y.; Powell, K.A.; Liu, Z.; Hunt, W.H.; Young, S.A. Overview of the CALIPSO Mission and CALIOP Data Processing Algorithms. *J. Atmos. Ocean. Technol.* **2009**, *26*, 2310–2323. Available online: https://journals.ametsoc.org/view/journals/atot/26/11/2009jtech1281_1.xml (accessed on 15 November 2023). [CrossRef]
41. Kim, M.-H.; Omar, A.H.; Tackett, J.L.; Vaughan, M.A.; Winker, D.M.; Trepte, C.R.; Hu, Y.; Liu, Z.; Poole, L.R.; Pitts, M.C.; et al. The CALIPSO version 4 automated aerosol classification and lidar ratio selection algorithm. *Atmos. Meas. Tech.* **2018**, *11*, 6107–6135. [CrossRef]
42. Vaughan, M.A.; Powell, K.A.; Winker, D.M.; Hostetler, C.A.; Kuehn, R.E.; Hunt, W.H.; Getzewich, B.J.; Young, S.A.; Liu, Z.; McGill, M.J. Fully Automated Detection of Cloud and Aerosol Layers in the CALIPSO Lidar Measurements. *J. Atmos. Ocean. Tech.* **2009**, *26*, 2034–2050. [CrossRef]
43. Liu, Z.; Kar, J.; Zeng, S.; Tackett, J.; Vaughan, M.; Avery, M.; Pelon, J.; Getzewich, B.; Lee, K.-P.; Magill, B.; et al. Discriminating between Clouds and Aerosols in the Caliop Version 4.1 Data Products. *Atmos. Meas. Tech.* **2019**, *12*, 703–734. [CrossRef]
44. Tackett, J.L.; Kar, J.; Vaughan, M.A.; Getzewich, B.J.; Kim, M.-H.; Vernier, J.-P.; Omar, A.H.; Magill, B.E.; Pitts, M.C.; Winker, D.M. The CALIPSO version 4.5 stratospheric aerosol subtyping algorithm. *Atmos. Meas. Tech.* **2023**, *16*, 745–768. [CrossRef]
45. Taha, G. OMPS-NPP L2 LP Aerosol Extinction Vertical Profile Swath Daily 3slit V2, Greenbelt, MD, USA, Goddard Earth Sciences Data and Information Services Center (GES DISC). 2020. Available online: https://disc.gsfc.nasa.gov/datasets/OMPS_NPP_LP_L2_AER_DAILY_2/summary (accessed on 2 May 2023).
46. Chen, Z.; Bhartia, P.K.; Loughman, R.; Colarco, P.; DeLand, M. Improvement of stratospheric aerosol extinction retrieval from OMPS/LP using a new aerosol model. *Atmos. Meas. Tech.* **2018**, *11*, 6495–6509. [CrossRef] [PubMed]
47. Taha, G.; Loughman, R.; Colarco, P.R.; Zhu, T.; Thomason, L.W.; Jaross, G. Tracking the 2022 Hunga Tonga-Hunga Ha’apai aerosol cloud in the upper and middle stratosphere using space-based observations. *Geophys. Res. Lett.* **2022**, *49*, e2022GL100091. [CrossRef] [PubMed]
48. Taha, G.; Loughman, R.; Zhu, T.; Thomason, L.; Kar, J.; Rieger, L.; Bourassa, A. OMPS LP Version 2.0 multi-wavelength aerosol extinction coefficient retrieval algorithm. *Atmos. Meas. Tech.* **2021**, *14*, 1015–1036. [CrossRef]
49. Kloss, C.; Berthet, G.; Sellitto, P.; Ploeger, F.; Taha, G.; Tidiga, M.; Efremenko, M.; Bossolasco, A.; Jégou, F.; Renard, J.-B.; et al. Stratospheric aerosol layer perturbation caused by the 2019 Raikoke and Ulawun eruptions and their radiative forcing. *Atmos. Chem. Phys.* **2021**, *21*, 535–560. [CrossRef]
50. Gorkavyi, N.; Krotkov, N.; Li, C.; Lait, L.; Colarco, P.; Carn, S.; DeLand, M.; Newman, P.; Schoeberl, M.; Taha, G.; et al. Tracking aerosols and SO₂ clouds from the Raikoke eruption: 3D view from satellite observations. *Atmos. Meas. Tech.* **2021**, *14*, 7545–7563. [CrossRef]
51. Wells, A.F.; Jones, A.; Osborne, M.; Damany-Pearce, L.; Partridge, D.G.; Haywood, J.M. Including ash in UKESM1 model simulations of the Raikoke volcanic eruption reveals improved agreement with observations. *Atmos. Chem. Phys.* **2023**, *23*, 3985–4007. [CrossRef]
52. Peuch, V.; Engelen, R.; Rixen, M.; Dee, D.; Flemming, J.; Suttie, M.; Ades, M.; Agustí-Panareda, A.; Ananasso, C.; Andersson, E.; et al. The Copernicus Atmosphere Monitoring Service: From research to operations. *Bull. Am. Meteorol. Soc.* **2022**, *103*, E2650–E2668. [CrossRef]
53. Inness, A.; Ades, M.; Balis, D.; Efremenko, D.; Flemming, J.; Hedelt, P.; Koukouli, M.-E.; Loyola, D.; Ribas, R. Evaluating the assimilation of S5P/TROPOMI near real-time SO₂ columns and layer height data into the CAMS integrated forecasting system (CY47R1), based on a case study of the 2019 Raikoke eruption. *Geosci. Model Dev.* **2022**, *15*, 971–994. [CrossRef]
54. Hedelt, P.; Efremenko, D.S.; Loyola, D.G.; Spurr, R.; Clarisse, L. Sulfur dioxide layer height retrieval from Sentinel-5 Precursor/TROPOMI using FP_ILM. *Atmos. Meas. Tech.* **2019**, *12*, 5503–5517. [CrossRef]

55. Koukouli, M.-E.; Michailidis, K.; Hedelt, P.; Taylor, I.A.; Inness, A.; Clarisse, L.; Balis, D.; Efremenko, D.; Loyola, D.; Grainger, R.G.; et al. Volcanic SO₂ layer height by TROPOMI/S5P: Evaluation against IASI/MetOp and CALIOP/CALIPSO observations. *Atmos. Chem. Phys.* **2022**, *22*, 5665–5683. [[CrossRef](#)]
56. Yarwood, G.; Rao, S.; Yocke, M.; Whitten, G.Z. *Updates to the Carbon Bond Mechanism: CB05. Final Report to the US Environmental Protection Agency*; RT-0400675; Yocke and Company: Novato, CA, USA, 2005.
57. Huijnen, V.; Williams, J.; van Weele, M.; van Noije, T.; Krol, M.; Dentener, F.; Segers, A.; Houweling, S.; Peters, W.; de Laat, J.; et al. The global chemistry transport model TM5: Description and evaluation of the tropospheric chemistry version 3.0. *Geosci. Model Dev.* **2010**, *3*, 445–473. [[CrossRef](#)]
58. Mann, G.W.; Carslaw, K.S.; Spracklen, D.V.; Ridley, D.A.; Manktelow, P.T.; Chipperfield, M.P.; Pickering, S.J.; Johnson, C.E. Description and evaluation of GLOMAP-mode: A modal global aerosol microphysics model for the UKCA composition-climate model. *Geosci. Model Dev.* **2010**, *3*, 519–551. [[CrossRef](#)]
59. Huijnen, V.; Flemming, J.; Chabirillat, S.; Errera, Q.; Christophe, Y.; Blechschmidt, A.-M.; Richter, A.; Eskes, H. C-IFS-CB05-BASCOE: Stratospheric chemistry in the Integrated Forecasting System of ECMWF. *Geosci. Model Dev.* **2016**, *9*, 3071–3091. [[CrossRef](#)]
60. Cameron, W.; Bernath, D.P.; Boone, C. Sulfur dioxide from the atmospheric chemistry experiment (ACE) satellite. *J. Quant. Spectrosc. Radiat. Transf.* **2021**, *258*, 107341. [[CrossRef](#)]
61. Ansmann, A.; Ohneiser, K.; Chudnovsky, A.; Baars, H.; Engelmann, R. CALIPSO Aerosol-Typing Scheme Misclassified Stratospheric Fire Smoke: Case Study From the 2019 Siberian Wildfire Season. *Front. Environ. Sci.* **2021**, *9*, 769852. [[CrossRef](#)]
62. Hoffmann, L.; Spang, R. An assessment of tropopause characteristics of the ERA5 and ERA-Interim meteorological reanalyses. *Atmos. Chem. Phys.* **2022**, *22*, 4019–4046. [[CrossRef](#)]
63. Michailidis, K.; Siomos, N.; Balis, D. Performance of the Aerosol Species Separation Algorithm (ASSA) Using Data from a Raman-Depolarization Lidar System at Thessaloniki, Greece. *Environ. Sci. Proc.* **2023**, *26*, 70. [[CrossRef](#)]

Disclaimer/Publisher’s Note: The statements, opinions and data contained in all publications are solely those of the individual author(s) and contributor(s) and not of MDPI and/or the editor(s). MDPI and/or the editor(s) disclaim responsibility for any injury to people or property resulting from any ideas, methods, instructions or products referred to in the content.